3-D Volume Reconstruction of Skin Lesions for Melanin and Blood Volume Estimation and Lesion Severity Analysis

Brian D'Alessandro, Atam P. Dhawan, *Fellow, IEEE*

***Abstract*—Subsurface information about skin lesions, such as the blood volume beneath the lesion, is important for the analysis of lesion severity towards early detection of skin cancer such as malignant melanoma. Depth information can be obtained from diffuse reflectance based multispectral transillumination images of the skin. An inverse volume reconstruction method is presented which uses a genetic algorithm optimization procedure with a novel population initialization routine and nudge operator based on the multispectral images to reconstruct the melanin and blood layer volume components. Forward model evaluation for fitness calculation is performed using a parallel processing voxel-based Monte Carlo simulation of light in skin. Reconstruction results for simulated lesions show excellent volume accuracy. Preliminary validation is also done using a set of 14 clinical lesions, categorized into lesion severity by an expert dermatologist. Using two features, the average blood layer thickness and the ratio of blood volume to total lesion volume, the lesions can be classified into mild and moderate/severe classes with 100% accuracy. The method therefore has excellent potential for detection and analysis of pre-malignant lesions.**

***Index Terms*—transillumination, multispectral imaging, melanoma, hemoglobin, volume reconstruction, skin lesions, dermoscopy**

I. Introduction

MALIGNANT melanoma is expected to result in over 9,100 deaths in 2012 [1], but the survival rate is quite high if the cancer is detected early. Hence, the early detection of malignant skin lesions is critical to preventing death. Conventional analysis of suspicious skin lesions involves visual examination by a trained expert aided with surface lighting and magnification to analyze the visible structure of a nevus [2]. However, the deeper pigmentation structure is often overcome by the surface light reflection, and thus, important information regarding the depth extent of the malignancy is obscured. Deeper subsurface information, such as indications of increased blood flow (angiogenesis) are critical factors in early melanoma detection [3]. As a result, much effort is being put into the evaluation of novel noninvasive optical imaging techniques as a way to detect and analyze the morphological changes associated with tumorigenesis, thereby improving patient diagnosis accuracy with minimal need for invasive and time consuming biopsy procedures.

Advanced optical imaging modalities including optical coherence tomography and confocal microscopy have been investigated for skin lesion imaging [4], [5]. However, these imaging technologies are still expensive and may require specialized training to read the resulting images [6]. Small, inexpensive hand-held devices such as the DermLite or DermScope illuminate a skin lesion with polarized light, thus greatly reducing specular reflection. However, diagnosis of the lesions imaged is still left up to the physician, which is subjective and therefore can vary significantly. Accuracy of diagnosis also decreases for non-expert physicians who do not specialize in melanoma detection [7]. Furthermore, the use of white light does not allow for accurate depth and chromophore analysis.

As a result, there has been much investigation into computer aided analysis of dermoscopy images, some even utilizing multispectral imaging [8]–[10]. However, many of these methods only propose to differentiate between malignant and benign skin lesions, but do not identify any early indicators of lesion severity such as angiogenesis which could lead to an early diagnosis of skin cancer. Other work has been performed to separate out melanin and blood contents of the skin, using techniques such as ICA [11] or the differential modified Beer–Lambert law [12], but these do not have the goal of melanoma and lesion severity detection, nor do they attempt to reconstruct the volumetric measurements of skin lesions, or the blood present beneath these skin lesions, which is a much more difficult problem. Other methods to map erythema, such as Tissue Viability Imaging even produce false red blood cell concentration values at the locations of pigmented lesions [13].

MelaFind, a commercial device, aggregates multispectral features into a single "disorganization" factor which is intended to aid a trained dermatologist in the decision to biopsy [14]. However, the specificity is low (9.9%). SIAscopy, on the other hand, claims to separate out melanin, blood, dermal melanin, and collagen from a series of multispectral images in the infrared and near infrared range [15], [16]. The method is based on Kubelka-Munk theory of a homogenous layered skin model to find a tissue color to histological parameter mapping, which is then applied pixel-by-pixel in the acquired images. However, this may not capture diffuse light interactions of heterogeneous lesion tissue or the point spread function (PSF) of deeper tissue [17].

Additionally, the dermoscopy techniques discussed above use surface illumination. Even if cross-polarization is used,

Brian D'Alessandro (email: bmd5@njit.edu) and Atam P. Dhawan (email: dhawan@njit.edu) are with the Department of Electrical and Computer Engineering, New Jersey Institute of Technology, Newark, NJ 07102 USA.

Copyright (c) 2012 IEEE. Personal use of this material is permitted. However, permission to use this material for any other purposes must be obtained from the IEEE by sending a request to pubs-permissions@ieee.org.

IEEE Transactions on Medical Imaging, vol. 31, no. 11, pp. 2083-2092, 2012

Digital Object Identifier 10.1109/TMI.2012.2209434

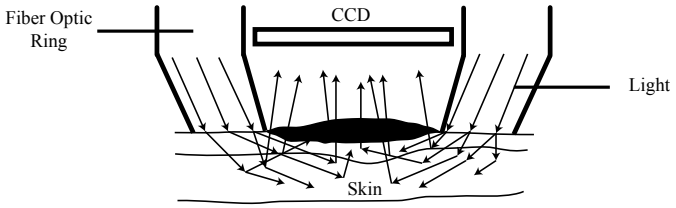

Fig. 1. Light pathways of diffuse reflectance imaging (transillumination).

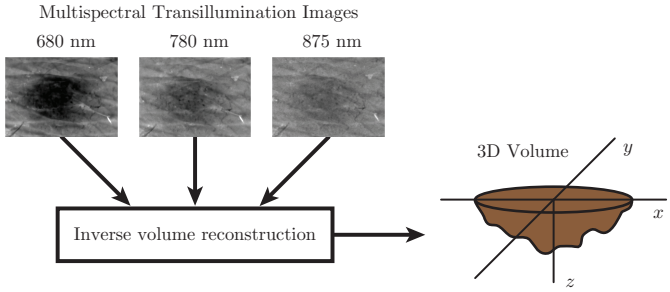

Fig. 2. Objective of the inverse reconstruction algorithm.

the majority of surface light is reflected back within the first few layers of skin, which limits the visualization of deeper structures. To overcome this limitation, a device known as the Nevoscope utilizes transillumination light microscopy (TLM) for imaging skin lesions. The Nevoscope contains a fiber optic ring light source that is placed against the skin. Light diffuses through the skin tissue beneath the lesion through scattering and absorption events, forming a backscattered transilluminated image of light which scatters up from behind the lesion (see Fig. 1). As a result, TLM imaging is able to visualize subsurface information more effectively by completely blocking surface illumination. Furthermore, images can be obtained using a multispectral light source, thus providing additional depth and chromophore information through multispectral imaging.

The goal of this work, then, is to reconstruct a 3D volume estimate of the skin lesion from TLM images (see Fig. 2). This is known as the inverse model of imaging. The forward model of imaging takes a known volume structure, and finds the multispectral TLM images. This forward model can be simulated through the use of a Monte Carlo simulation of light propagation in skin [18]. Previously, the inverse model was attempted by using Taylor series expansion to approximate the forward model using the first derivative (Jacobian) and matrix multiplication [19]. Since a large number of forward model executions are needed to evaluate the inverse model, this was done for reasons of speed. Once the initial Jacobian matrix is pre-computed through Monte Carlo simulation, subsequent forward model executions merely involve matrix multiplication, a computationally inexpensive operation. The downside is that this forward model approximation substantially increases in error the further away the point of evaluation deviates from the point of approximation. However, the authors have instead developed a voxel-based parallel processing Monte Carlo simulation of light in the skin, which is substantially faster than previously possible [20] and far more accurate than Taylor series approximation. Other researchers have used optimization with MCML [18] to reconstruct skin parameters [21]–[23], but the use of MCML requires the assumption that skin layers are homogenous. While this may be useful for certain skin conditions such as port wine stain, erythema, or global inflammation, it is not applicable for analysis of highly spatially-variant skin lesions.

With the voxel-based Monte Carlo method, the forward imaging model is well defined for simulation. However, the inverse model is much more difficult to find, and is ill-posed, meaning there are possibly many solutions. Since the subsurface 3D volume of a lesion is unknown, the multispectral Nevoscope image set is used to reconstruct an estimate of the volume with depth and chromophore information. Hence, although imaging is not performed tomographically, volumetric estimates are made based on the topographic multispectral images. The most common chromophores encountered in the skin are melanin and the main components of blood: oxygenated hemoglobin and deoxygenated hemoglobin. It is the absorption coefficient, μ_a, at individual locations within the tissue volume which give critical information about the three-dimensional distribution and depth of the lesion, size of the blood volume, as well as the relative amounts of the major chromophores. Thus, the problem is to find the unknown voxel grid of $\mu_a(x, y, z)$, which when passed through the forward model, produces images which are closest to the actual images obtained from the Nevoscope. This is an optimization problem which can be solved by numerous methods, one of which is through a genetic algorithm (GA).

An initial estimate of the 3D skin lesion volume is made based on the *a priori* characteristics extracted from the multispectral transilluminated image set. This initial estimate is then used as a seed to generate a population of volume solutions which are randomized around that initial estimate. This population of solutions then proceeds through a GA-based optimization process to iteratively reconstruct an optimal solution within a wide to an increasingly narrow search space. Features from this optimal reconstructed volume, such as depth, melanin volume, and blood volume, are extracted as features for lesion severity classification. Through the novel techniques described in this paper, a parallel processing Monte Carlo simulation, as well as a novel GA initialization routine and operator based on knowledge gained from the multispectral images, the accuracy of lesion volume reconstruction is substantially improved over previous work. Furthermore, a set of 14 clinical lesions have been analyzed for the first time, for a preliminary validation of the methods discussed. The proposed methodology has many benefits over other skin lesion analysis methods, including the use of a voxel-based Monte Carlo simulation which simulates irregularly shaped lesions and heterogeneous skin layers with spatially variant chromophore distributions, use of the ring geometry of the Nevoscope which allows for improved depth information recovery, as well as a correspondence of our recovered features to lesion severity with an aim towards early diagnosis, not just a benign/malignant differentiation.

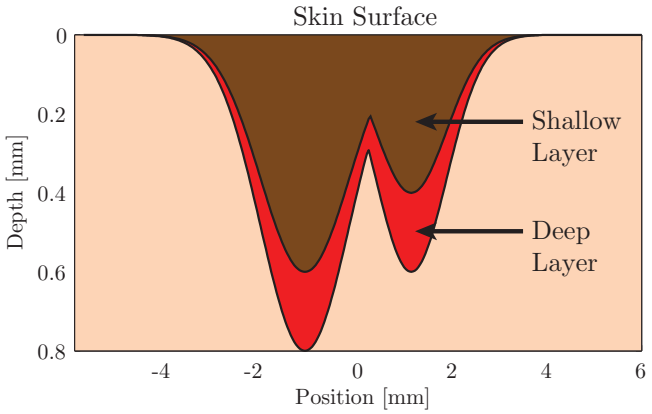

Fig. 3. The two-layered skin lesion model. The shallow layer consists of melanin while the deep layer consists of blood.

II. Two-Layered Skin Model

It is well-known that a pigmented skin lesion consists of additional melanin compared to the background skin. Furthermore, a skin lesion may possess a distinct vascular pattern beneath the lesion. This network of blood vessels is more prevalent in malignant lesions than in benign lesions [3]. With this in mind to assist in reconstruction, a two-layered skin lesion model is implemented (see Fig. 3). The volume bounded by the skin surface and the shallow layer boundary consists of some volume fraction of melanin C_{M}, while the volume bounded by the shallow layer boundary and the deep layer boundary consists of some volume fraction of blood C_{B}. Such a simplified two-layered model has been used before in lesion reconstruction [19]. The blood layer contains a mixture of Hb and HbO_2 depending on the oxygen saturation level, $[SO_2]$. These chromophore volume fraction parameters can be used with their known chromophore absorption coefficients to find the specific μ_a values of each layer [24], [25]:

$$\mu_a^{\mathrm{BG}}(\lambda) = (1 - C_{\mathrm{M}} - C_{\mathrm{B}})\,\mu_a^{\text{baseline}}(\lambda) \quad (1)$$

$$\mu_a^{\mathrm{ML}}(\lambda) = C_{\mathrm{M}}\mu_a^{\text{melanin}}(\lambda) \quad (2)$$

$$\mu_a^{\mathrm{BL}}(\lambda) = C_{\mathrm{B}}\left([\mathrm{SO}_2]\mu_a^{\mathrm{HbO}_2}(\lambda) + (1 - [\mathrm{SO}_2])\,\mu_a^{\mathrm{Hb}}(\lambda)\right) \quad (3)$$

where μ_a^{BG}, μ_a^{ML}, and μ_a^{BL} are the absorption coefficients of the background skin, melanin layer, and blood layer respectively.

In order to simulate this lesion model, a Monte Carlo based forward model of imaging is utilized. The lesion is discretized into a three dimensional voxel grid, where each voxel allows for an individual set of wavelength-dependent optical properties such as the absorption coefficient $\mu_a(\lambda)$, the scattering coefficient $\mu_s(\lambda)$, and the anisotropy factor $g(\lambda)$. While reported values vary, both μ_s and g can be assumed to be approximately equal in the epidermis and dermis [24], [26], and can be represented in terms of the reduced scattering coefficient μ_s' as a combination of Mie scattering and Rayleigh scattering by:

$$\mu_s(\lambda) = \mu_s'(\lambda)/(1 - g(\lambda)) \quad (4)$$

$$\mu_s'(\lambda) = 2 \cdot 10^5 \lambda^{-1.5} + 2 \cdot 10^{12}\lambda^{-4}\ [\mathrm{cm}^{-1}] \quad (5)$$

$$g(\lambda) = 0.62 + 0.29 \cdot 10^{-3} \cdot \lambda \quad (6)$$

To simulate the forward imaging model, individual photons of light are propagated through the defined voxel volume. Photons enter the volume at a random location within a 0.5 mm wide ring light source with an outer diameter of 1.175 cm. The photons are initially directed at a 45° angle downwards towards the center of the ring.

Well-known equations govern the step lengths, intensity reduction, and scattering angles of these discrete photons as they traverse through each voxel, which are dependent on the optical properties of that voxel [18]. Photons which backscatter through the skin surface add to the diffuse reflectance image. Simulating millions of these photons is necessary to average the light path through the tissue volume and lesion in order to obtain a simulated transillumination image of backscattered light at the surface. Since these photons are simulated independently of each other, they are highly amenable to parallel processing on a desktop graphics card. Simulation of 10 million photons using the Monte Carlo simulation from Wang et al. [19] took 1 hour and 13 minutes on a 3.16 GHz dual core CPU, whereas the GPU-enhanced simulation took only 1.29 seconds [20]. This speed improvement of over $3000\times$ allows a higher accuracy of Nevoscope simulation than what was previously possible from Taylor series expansion of the Monte Carlo forward model [19], since the Monte Carlo forward model can be used directly rather than simply a first-order approximation of it. To illustrate the errors possible in a first-order Taylor series forward model approximation, a $0.5\times0.5\times0.1$ cm^3 object was embedded in the top layer of a virtual volume at the center of the illumination ring. Images produced by the approximation were compared with "true" images produced by direct Monte Carlo simulation. In both cases, 100 million photons were simulated. When approximating the Taylor series around a background μ_a of 0.25 cm^{-1}, less than 10% error was observed when μ_a of the object = 1.5 cm^{-1}. However, as μ_a increased past 3.5 cm^{-1}, the error exceeded 50%. Clearly, the loss of accuracy using Taylor series approximation is substantial. Direct use of the Monte Carlo simulation in inverse reconstruction was previously impossible, as it would have required an inordinate amount of time. However, the parallel GPU-based Monte Carlo simulation solves this problem. In this way, accurate simulated Nevoscope transillumination images can be obtained for lesions of any size, shape, and composition in an acceptable amount of time.

III. Initial Volume Estimate

A good initial volume estimate is highly beneficial for a faster and more accurate final volume search through genetic algorithm optimization. By using the Monte Carlo simulation forward model, a Beer's law correction factor, specific to the Nevoscope geometry, was estimated in order to relate the pixel intensity seen in the surface TLM images to the absorption coefficient and depth of an embedded object adjacent to the skin surface. Details of this procedure are discussed in [27], [28], but to summarize, an equation of the form $I/I_0 = f(\mu_a, \ell)$ was developed where I is a pixel intensity

TABLE I
RATIO OF MELANIN ABSORPTION TO BLOOD ABSORPTION

Wavelength (nm)	$\mu_a^{\text{melanin}}/\mu_a^{\text{blood}}$
600	2.87
680	14.97
780	9.54
800	8.75
875	4.94

Values displayed for C_{M}=5%, C_{B}=20%, and $[\text{SO}_2]$=75%.

value in an image with the object, I_0 is the intensity of the same pixel in the background image without the object, μ_a is absorption coefficient of the object, and ℓ is the depth of the object. Scattering was assumed to be constant. The function was approximated by $f(\mu_a, \ell) \sim \exp(R(\mu_a, \ell))$ where $R(\mu_a, \ell)$ was fit through Monte Carlo simulation over a range of values for μ_a and ℓ. If this correction function f is written as $I/I_0 = f(\mu_a, \ell)$, then an inverse function to approximate the object depth ℓ at pixel location (x, y) can be produced by:

$$\ell(x, y) = f^{-1}\left(\mu_a, \frac{I}{I_0}\right) \tag{7}$$

To estimate the thickness of the melanin layer, ℓ^{ML}, the wavelength is used where the ratio of the absorption of melanin to the absorption of blood is greatest. Within the range of wavelength filters which were used for imaging (600, 680, 780, and 875 nm), 680 nm provides the largest $\mu_a^{\text{melanin}}/\mu_a^{\text{blood}}$ ratio (see Table I for an example). Imaging at this wavelength can be roughly assumed to visualize melanin alone. Thus, the initial estimate of the melanin layer thickness in the two-layered skin lesion model is:

$$\ell^{\text{ML}}(x, y) = f^{-1}\left(\mu_a^{\text{ML}}(680), \frac{I}{I_0}(680)\right) \tag{8}$$

To find an estimate of the blood layer thickness, the wavelength with the smallest $\mu_a^{\text{melanin}}/\mu_a^{\text{blood}}$ ratio is similarly used, 600 nm. However, melanin is still a large component of the absorption image at this wavelength and must be canceled out. The solution of $\ell_{600}^{\text{ML}}(x, y) = f^{-1}\left(\mu_a^{\text{ML}}(600), \frac{I}{I_0}(600)\right)$ provides the estimated thickness of the lesion as if it were 100% melanin. Subtracting the previous result for $\ell^{\text{ML}}(x, y)$ results in the difference in thickness measurements, presumably due to the presence of blood. However, since this blood thickness has been estimated with an absorption coefficient of $\mu_a^{\text{ML}}(600)$, the thickness must be modified accordingly by the ratio of $c = \mu_a^{\text{ML}}(600)/\mu_a^{\text{BL}}(600)$. Thus, the initial estimate of the blood layer thickness $\ell^{\text{BL}}(x, y)$ is:

$$\ell^{\text{BL}}(x, y) = c \cdot \left(\ell_{600}^{\text{ML}}(x, y) - \ell^{\text{ML}}(x, y)\right) \tag{9}$$

These estimates of $\ell^{\text{ML}}(x, y)$ and $\ell^{\text{BL}}(x, y)$ are adequate but can still be improved further. The surface imaging response of objects within the skin has a specific wavelength and depth-dependent point spread function [17]. Knowledge of this point spread function can be used to deconvolve the initial volume estimate at each depth interval in the voxel grid.

To that end, the PSF of objects within the Monte Carlo simulated volume was determined. To find the PSFs of objects at various voxel grid depths z simulated by the Monte Carlo simulation, slabs one voxel thick of large absorption were embedded in a virtual volume taking up half of the imaging field of view. This allows for an accurate measurement of the depth and wavelength dependent edge spread function, $\text{ESF}(z, \lambda)$, from which the PSFs were derived mathematically [29]–[31]. Since the 2D PSFs are also a function of (x, y), the whole set is denoted as $\text{PSF}(x, y, z, \lambda)$.

Knowing $\text{PSF}(x, y, z, \lambda)$, deconvolution of the layer depth estimates can proceed. Initially, a depth estimate $\ell(x, y)$ is converted to a binary volume $L_0(x, y, z)$ such that a 1 represents the presence of an absorber in voxel (x, y, z) and a 0 represents the absence of an absorber:

$$\forall z \in \mathbb{N}_1 : \; L_0(x, y, z) = \begin{cases} 1 & \text{if } z \leq \ell(x, y) \\ 0 & \text{otherwise} \end{cases} \tag{10}$$

With this initial volume model, each z layer is deconvolved. The residual of each deconvolution is then projected to the next deepest layer, resulting in the final deconvolved binary volume model $L_f(x, y, z)$. This procedure can be written as:

$$L_f(x, y, z) = \min(\lfloor L_i(x, y, z) *^{-1} \text{PSF}(x, y, z, \lambda) \rceil, 1) \tag{11}$$

where:

$$\begin{aligned} L_i(x, y, z) &= L_0(x, y, z) + \epsilon(x, y, z - 1) \\ \epsilon(x, y, z) &= \max(\lfloor L_i(x, y, z) *^{-1} \text{PSF}(x, y, z, \lambda) \rceil - 1, 0) \\ \epsilon(x, y, 0) &= 0 \end{aligned}$$

and $*^{-1}$ denotes Wiener deconvolution with a signal-to-noise ratio (SNR) of 6.25. This value was calculated empirically and was found to work acceptably well at deconvolution across the utilized wavelength and depth ranges.

The above process is performed on ℓ^{ML} and $\ell^{\text{ML+BL}}$ where $\ell^{\text{ML+BL}} = \ell^{\text{ML}} + \ell^{\text{BL}}$. This produces $L_f^{\text{ML}}(x, y, z)$ and $L_f^{\text{ML+BL}}(x, y, z)$ as the deconvolved binary volumes. Next, $L_f^{\text{BL}}(x, y, z) = L_f^{\text{ML+BL}}(x, y, z) - L_f^{\text{ML}}(x, y, z)$ is found, and the binary volumes for both the melanin and blood layers are converted back to thickness maps:

$$\ell_f(x, y) = \sum_z L_f(x, y, z) \tag{12}$$

Minimum and maximum value constraints are imposed on the thickness of each of these volumes such that $\ell_{\text{max}}^{\text{ML}}$ and $\ell_{\text{max}}^{\text{BL}}$ are the maximum thickness of the melanin and blood layer, respectively, resulting in the final thickness maps, ℓ_f^{ML} and ℓ_f^{BL}, for the melanin and blood layers of the initial volume estimate.

Furthermore, since the original set of model parameters (C_{M}, C_{B}, and $[\text{SO}_2]$) had fixed assumed values, the initial volume estimate and GA reconstruction procedure must be performed for each combination of parameter values within a desired range. The final estimated set of parameters is selected based upon the solution that produces the highest fitness.

IV. GENETIC ALGORITHM FOR 3D RECONSTRUCTION

While the initial volume estimate provides a good "first guess" at the shape of the subsurface lesion and the size of the melanin and blood layers, a number of assumptions are involved which can lead to inaccurate estimates. Consequently,

a more robust reconstruction must be undertaken while aided by knowledge of the initial volume estimate. Since the 3D reconstruction process is ill-posed, a GA-based optimization process is used to search the solution space for an optimal solution [32].

A. Population Initialization

The GA for volume reconstruction begins by initializing a population of proposed solutions. Each proposed solution is encoded as a "chromosome" for use during the GA. The chromosome for one particular individual in the population is defined by both the melanin and blood thickness maps. For example, the chromosome for the initial volume estimate (henceforth known as the model chromosome) is defined as the set $\{\ \ell_f^{\mathrm{ML}},\quad \ell_f^{\mathrm{BL}}\ \}$. The values in each chromosome, known as alleles, represent the thickness of the respective chromophores. Since these thickness values are equivalent to the number of voxels in the z direction, chromosome alleles are always whole numbers. To further assist the reconstruction process, a mask is defined to ignore reconstruction at (x, y) locations where the lesion is not present. Thus, a lesion ROI is defined as a binary mask $m(x, y)$, and is segmented manually from the acquired images.

Members of the GA population are varied around the model chromosome according to three categories, selected at random for each member. For the shallow bias category, each allele has a 15% chance of decreasing by 1 (meaning the depth at that position becomes shallower), an 80% of not changing, and a 5% chance of increasing by 1 (the depth becomes deeper). For the no bias category, the chances are 10%, 80%, and 10%, respectively. For the deep bias category, the chances are 5%, 80%, and 15%, respectively. In this manner, population variability is maintained, but each chromosome is based on the model chromosome.

B. Fitness Evaluation

Chromosomes are evaluated as to their fitness by executing the forward model on the chromosome, and then comparing the forward model simulated TLM images with the real TLM images. In order to run the Monte Carlo simulation on a given chromosome $\{\ \ell^{\mathrm{ML}},\quad \ell^{\mathrm{BL}}\ \}$, the thickness maps within that chromosome are converted into a voxel volume with correct absorption coefficients for the wavelength simulated. Propagation of light through this volume is then simulated. The fitness F of each chromosome is then evaluated by a comparison between the multispectral images of the true lesion ($I_\lambda^{\mathrm{real}}$) and the images generated by the forward model simulation (I_λ) on that chromosome, within the defined mask:

$$F = -\ln\left(\frac{1}{N_\lambda N_\ell}\sum_{\lambda,x,y}\frac{|I_\lambda(x,y) - I_\lambda^{\mathrm{real}}(x,y)|}{I_\lambda^{\mathrm{real}}(x,y)}m(x,y)\right) \tag{13}$$

where N_λ is the number of wavelengths used for imaging, and N_ℓ is the number of depth points within the mask such that $N_\ell = \sum_{x,y} m(x, y)$.

C. Genetic Algorithm Operators

Once the population of chromosomes is initialized, the GA proceeds by altering this population through a set of reproduction operators. The implemented GA for volume reconstruction uses steady state reproduction without duplicates, uniform crossover, random mutation, nudge mutation, and a novel intelligent nudge operator. Chromosomes are selected for reproduction by a roulette wheel with rank normalization on the fitness. The random mutation operator gives each allele in the selected chromosome a 0.8% chance of mutating to a random new value within the layer thickness constraints. The nudge mutation operator mutates alleles only by $+1$ or -1 from their current value; the direction is chosen at random.

The proposed intelligent nudge operator is based on the hill-climbing optimization technique, but the selection of alleles to nudge is derived from knowledge of the chromophores involved and their effect on the multispectral images. It is designed such that a nudge mutation occurs only in the volume region which produces the maximum error between the simulated and true images. First, a difference map is found at 680 nm, representing the difference primarily due to errors in the melanin layer:

$$D_{680}(x, y) = I_{680}(x, y) - I_{680}^{\mathrm{real}}(x, y) \tag{14}$$

Next, the pixel location (i, j) of the maximum absolute value of this difference image is found:

$$(i, j) = \arg\max_{x,y}(|D_{680}(x, y)|) \tag{15}$$

Finally, the melanin layer thickness map of the roulette selected chromosome $\{\ \ell_0^{\mathrm{ML}},\quad \ell_0^{\mathrm{BL}}\ \}$ is adjusted by ± 1 depending on the necessary direction:

$$\ell^{\mathrm{ML}}(i, j) = \ell_0^{\mathrm{ML}}(i, j) + \mathrm{sgn}(D_{680}(i, j)) \tag{16}$$

The blood layer thickness map is also adjusted. A difference image is found at 600 nm, but since this difference image will still include error from the melanin layer, $D_{680}(x, y)$ is subtracted out, with adjustment made for the difference in melanin absorption coefficient between 600 and 680 nm:

$$\begin{aligned} D_{600}(x, y) \quad = \quad & \left[I_{600}(x, y) - I_{600}^{\mathrm{real}}(x, y)\right] \\ & -\frac{\mu_a^{\mathrm{ML}}(600) - \mu_a^{\mathrm{BG}}(600)}{\mu_a^{\mathrm{ML}}(680) - \mu_a^{\mathrm{BG}}(680)}D_{680}(x, y) \end{aligned} \tag{17}$$

As before, the location of the maximum difference due to blood error is found, and a nudge of ± 1 is made in the blood thickness map in the proper direction based on D_{600} to find ℓ^{BL}. Correct boundaries on the melanin and blood layers are enforced, the new chromosome $\{\ \ell^{\mathrm{ML}},\quad \ell^{\mathrm{BL}}\ \}$ is updated to find its new fitness, and the GA proceeds.

Only one operator is chosen for each generation, and the selection is made by a roulette. Additionally, the probability of selecting each operator is changed over the course of the GA. For example, an initial operator probability could be 80%, 10%, and 10% for crossover, mutate, and nudge respectively; but these could be linearly scaled towards 20%, 40%, and 40% by the final generation. The motivation for this is that a high crossover rate early in the GA is beneficial for initial exploration through the global search space. However, as the

population converges, a higher mutation rate is beneficial for improved local search. Furthermore, the number of photons used for simulation is interpolated from a low number to a higher number (for example, 1.5×10^6 to 3×10^6) over the course of the GA. The reason for this is to save computation time where possible: faster, but noisier images are acceptable initially during the global search stage, while images with a higher SNR are needed during the final stages of the GA to better differentiate chromosomes which vary only by small mutations. The number of generations for the GA was limited to the nearest thousand after the difference in fitness between the 100-generation moving average and the 10-generation moving average was less than 0.05%.

After the conclusion of the GA, the best lesion volume estimate, $\{\ \ell_{\text{best}}^{\text{ML}},\quad \ell_{\text{best}}^{\text{BL}}\ \}$, can then be evaluated to extract features to be used in a classifier for the detection of precancerous skin lesions.

V. Volume Reconstruction Results on Simulated Lesions

A. Reconstruction of a Two-Peaked Mixed Gaussian at 16×16

To test the accuracy of the proposed method for inverse volume reconstruction, an artificial lesion was simulated. Initially, the same model was used as in the prior work [19] for an accurate comparison of results. The model consists of a two-layered, two-peaked, mixed Gaussian lesion (whose defining equations are detailed in [19]; see Fig. 3) set within a 12×12×5 mm^3 volume of voxel dimensions 16×16×50 (for a voxel size of 0.75×0.75×0.1 mm^3), with C_{M}=5%, C_{B}=20%, and [SO_2]=75%. The use of a two-peaked Gaussian shape model allowed for sufficient spatial and depth variation in order to evaluate the reconstruction. The shallow layer was restricted to 0-0.6 mm ($\ell_{\text{max}}^{\text{ML}} = 6$) while the deep layer was restricted to 0-0.2 mm ($\ell_{\text{max}}^{\text{BL}} = 2$). Segmentation of the image to only the region of interest limited the number of depth control points to 35, significantly higher than the previous work which used only 9. Thus, each chromosome in the GA was of length (35 control points)·(2 layers) = 70. Volume error for the shallow melanin layer & deep blood layer (ΔV_{ML} and ΔV_{BL}) were calculated by:

$$\Delta V = \frac{|\sum_{x,y} \ell_{\text{best}}(x,y) - \sum_{x,y} \ell_{\text{true}}(x,y)|}{\sum_{x,y} \ell_{\text{true}}(x,y)} \qquad (18)$$

where ℓ_{best} is the thickness map for one layer in the best fit chromosome after the conclusion of the GA and ℓ_{true} represents the true thickness map for that layer from the lesion model. Results are presented in Table II.

The proposed method of using the parallel processing Monte Carlo simulation as the forward model (rather than a Taylor series approximation) during reconstruction was first evaluated using imaging at single wavelengths separately: 600, 680, 780, and 875 nm, followed by using a combination of all four wavelengths. For these cases, the GA population was initialized randomly and used the crossover and random mutation operators. Volume errors are listed in Table II(b). As can be seen, the improved forward model accuracy provides superior results to the previous Taylor series-based work [shown in Table II(a)] at both layers in all trials. Furthermore, evaluation using a multispectral imaging set of four wavelengths is superior to using imaging at single wavelengths alone.

TABLE II
Results Comparison for a Two-Peaked Gaussian Lesion Model

	Melanin Vol Error	Blood Vol Error	Time
(a) Previous approach			
Wang, et al. [19]; 580, 800 nm	2.68%	16.58%	–
(b) Random initialization, crossover, random mutation			
Proposed; 600 nm	1.18%	10.71%	3512 s
Proposed; 680 nm	0.62%	13.84%	3357 s
Proposed; 780 nm	0.64%	13.46%	3161 s
Proposed; 875 nm	0.52%	9.36%	3083 s
Proposed; 600, 680, 780, 875 nm	0.33%	3.57%	5609 s
(c) Intelligent initialization, crossover, random mutation			
Proposed; 600, 680, 780, 875 nm	0.00%	1.33%	5715 s
(d) Intelligent initialization, crossover, intelligent nudge			
Proposed; 600, 680, 780, 875 nm	0.00%	0.41%	3449 s

Reconstruction parameters: (a) see [19]. (b-c) 200 population size, 5000 generations, 1.5×10^6-3×10^6 photons, 80%-20% crossover rate, 10%-40% random mutation rate with mutation probability 0.8%, 10%-40% nudge rate. (d) 50 population size, 1000 generations, 3×10^6-12×10^6 photons, 40%-20% crossover rate, 10%-10% nudge rate, 50%-70% intelligent nudge rate.

The accuracy can be improved even further through use of the novel intelligent initialization procedure. For the same lesion model, the melanin volume error was reduced to 0%, with a mere 1.33% blood volume error [see Table II(c)]. Clearly, starting the GA population much closer to the search space where the solution lies results in a much higher accuracy with a similar execution time as random initialization.

The accuracy of volume reconstruction is improved even more through the inclusion of the intelligent nudge operator in the GA. With this operator, the melanin volume error is maintained at 0%, but the blood volume error is reduced to 0.41% [see Table II(d)]. Moreover, since the intelligent nudge operator brings such a benefit to the GA reconstruction, only 1000 generations need to be simulated to reach convergence, which reduces the execution time of the algorithm. The reason for the improvement in accuracy is that the intelligent nudge operator incorporates knowledge of the multispectral images in deciding which alleles to nudge, as opposed to the other operators (crossover, random mutation, and nudge mutation) which are blind to this specific application and function simply on evolutionary principles. A hybrid GA such as this, incorporating *a priori* knowledge of the specific problem, is bound to outperform a conventional GA. Most definitely then, the combination of intelligent initialization, crossover, and intelligent nudge within the GA is quite robust and highly accurate at reconstructing the unknown volume of a skin lesion based on multispectral transilluminated images.

B. Reconstruction of a Two-Peaked Mixed Gaussian at 32×32

Given such good results, reconstruction at a finer x-y resolution, 32×32, was then attempted. The z resolution was left at 50 voxels, resulting in a voxel size of 0.375×0.375×0.1 mm^3. To initialize the 32×32 GA population, several options were attempted:

1) Random initialization of the new GA population.

TABLE III
COMPARISON OF VARIOUS METHODS OF INITIALIZING A 32×32 GA

Initialization Method	Fitness	Melanin Vol Error	Blood Vol Error
Random	2.3641	32.12%	22.00%
Interp from 16×16, Bicubic	3.5184	6.62%	13.00%
Intelligent init, no deconv	3.8080	4.30%	23.00%
Intelligent init, with deconv	4.0967	0.66%	13.00%
True Volume	4.1738	0.00%	0.00%

The 16×16 solution used for interpolation was obtained from Table II(d). Chromosome fitness was calculated using 1.2×10^7 photons and averaged over five MC runs.

2) Interpolation of the solution obtained from the 16×16 reconstruction.
3) Generation of a completely new model chromosome using the method described in Section III.

The results of these methods are presented in Table III, which lists the fitness, melanin volume error, and blood volume error for the model chromosome generated by each method (a random chromosome was selected for the random initialization case), compared to the fitness for when true volume itself is run through the MC simulation a second time. Since the MC simulation inherently involves a measure of randomness, the simulated TLM images will be slightly different after repeated executions. This true volume fitness therefore represents a theoretical maximum limit on fitness imposed by the noise present in the simulation.

Not surprisingly, the random initialization results in the largest volume errors. Interpolation from the 16×16 solution was better, however, the best results came from recomputing an initial volume estimate for the 32×32 case. This initial volume estimate was tested with and without the deconvolution step. It is clear that deconvolving the estimate obtained from the corrected equation substantially improves the accuracy of the model chromosome, producing a fitness very close to the maximum fitness allowed by noise and a melanin volume error of nearly 0%. As these procedures are used to initialize a population for GA optimization, this error decreases further after the conclusion of the GA.

C. Reconstruction of Cuboid Lesions of Various Depths

Rectangular prism shaped lesions (cuboids) were also simulated to gain an understanding of the depth at which reconstruction could still be performed reliably. It is clear from the results in Table IV that reconstruction within 1 mm is reasonably good, especially for the melanin layer. However, as the depth of the lesion increases, the blood volume error also increases. As the lesion extends deeper into the skin, it is harder to estimate the deeper profile and composition.

D. Reconstruction of a Four-Peaked Mixed Gaussian

To vary the shape even more, two additional peaks were added to the 16×16 two-peak mixed Gaussian model, to create a four-peaked model visualized in Fig. 4. The reconstruction results were good, with a melanin volume error of 0.8% and a blood volume error of 9.38%. Fig. 4 shows both the true and reconstructed volumes for this four-peak model. The shapes match closely, with all four peaks visibly recovered during reconstruction, despite the peaks having been defined at different depths.

TABLE IV
CUBOID LESION RECONSTRUCTION RESULTS

Melanin Thickness	Blood Thickness	Melanin Vol Error	Blood Vol Error	Time
0.3 mm	0.1 mm	0.00%	0.00%	3946 s
0.6 mm	0.2 mm	0.00%	5.56%	3747 s
0.9 mm	0.3 mm	1.85%	12.04%	8044 s
1.2 mm	0.4 mm	0.69%	32.64%	8308 s

Reconstruction performed using 600, 680, 780, and 875 nm on lesions 4.5×4.5 mm^2 in the x-y dimension, C_M=5%, C_B=20%, and [SO_2]=75%. The voxel grid was of size 16×16×50, with a voxel resolution of 0.75×0.75×0.1 mm^3. The 0.3 mm and 0.6 mm melanin thickness cuboids were reconstructed using the same parameters as Table II(d) with $\ell_{\max}^{ML} = 6$, and $\ell_{\max}^{BL} = 2$. The 0.9 mm and 1.2 mm melanin thickness cuboids were also reconstructed using the same parameters, but for 3000 generations, $\ell_{\max}^{ML} = 12$, and $\ell_{\max}^{BL} = 4$.

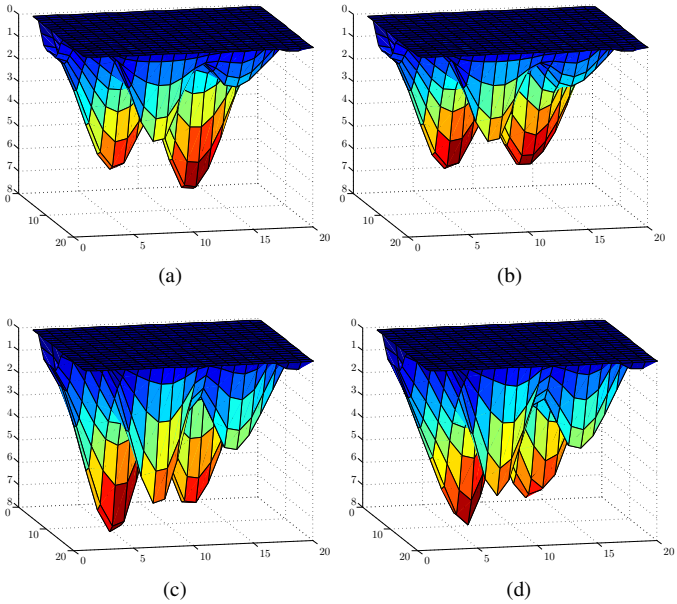

Fig. 4. Reconstruction results on the two-layered four-peaked Gaussian model. (a) Shallow surface true model and (b) reconstruction. (c) Deep surface true model and (d) reconstruction. Parameters: same as Table II(d).

E. Reconstruction with Varying Model Parameters

For real-world imaging, the true parameters, C_M, C_B, and [SO_2], would be unknown. To determine if these chromophore parameters could be recovered correctly based on selecting the parameter set which produces the highest fitness in the GA, reconstruction was re-run multiple times, each time changing the model parameters assumed during reconstruction. The two-peak Gaussian, cuboid, and four-peak Gaussian models were simulated with a true parameter set of C_M=5%, C_B=20%, and [SO_2]=75%. For all three models, C_M was varied between 4% and 6%, C_B was varied between 10% and 30%, and [SO_2] was fixed to 75%. Throughout this work, [SO_2] was assumed to be a constant in order to simplify the search space by reducing the number of variables to be solved. In future work, [SO_2] could also be a variable which is estimated during simulation similar to C_M and C_B. [SO_2] in melanoma lesions can vary

TABLE V
MODEL PARAMETERS VERSUS FINAL FITNESS

C_M	C_B 10%	C_B 20%	C_B 30%
4%	4.392	4.280	4.287
5%	4.695	4.745	4.598
6%	3.975	3.947	4.049

(a) Two-Peaked Lesion Model

C_M	C_B 10%	C_B 20%	C_B 30%
4%	4.201	4.196	4.186
5%	4.216	4.236	4.213
6%	4.203	4.183	4.193

(b) Cuboid Lesion Model

C_M	C_B 10%	C_B 20%	C_B 30%
4%	2.660	2.693	2.712
5%	3.435	3.471	3.354
6%	3.103	3.108	3.081

(c) Four-Peaked Lesion Model

Reconstruction parameters: population size of one with intelligent initialization, 10 generations, 100% intelligent nudge operator, 3×10^6-17×10^6 photons. (a-b) used a $16\times16\times50$ voxel grid, while (c) used a $32\times32\times50$ voxel grid. The cuboid volume of (b) was of size 3×3 mm^2 in the x-y dimension with a melanin thickness of 0.3 mm and a blood thickness of 0.1 mm. All models has a true C_M=5% and true C_B=20%.

by as much as -16% with respect to the surrounding skin, indicating hypoxia [33]. Thus, parallel efforts are ongoing to estimate blood oxygen saturation using transillumination imaging with the Nevoscope as a useful indicator of severity and early malignancy [17], [27], [28].

As can be seen in Table V, for each lesion model shape, high reconstruction fitness results when the correct C_M is used, even when C_B is incorrect. This makes sense as the melanin layer is closest to the surface and therefore has a large effect on the fitness; errors in the deeper blood layer contribute less to the fitness and so C_B is more difficult to detect. However, fitness is highest for C_M=5% and C_B=20%, which matches the parameters used in the true volume. As a result, by running the reconstruction with different initial assumptions, the correct parameters can be estimated by selecting the case which results in simulated images with a superior similarity to the true images.

VI. VOLUME RECONSTRUCTION RESULTS ON A SKIN PHANTOM

As an intermediate validation step, the reconstruction algorithm was run on Nevoscope transillumination images acquired on a skin phantom which was constructed to closely match the optical properties of human skin [34]. The main objective of the physical phantom was to validate the Nevoscope depth-dependent imaging for visualization and analysis of an embedded object in a skin tissue like medium with the capability of separation of Hb and HbO_2 in a mixture within a vascular structure (capillary tubes were used to represent vascularity in a very simple way) [17]. Considering that the medium had melanin spectral characteristics and the tubes could contain Hb and HbO_2, the phantom represented a tissue vascular structure with blood composition at a specific depth level. The Nevoscope imaging was evaluated and then used in validating the Monte Carlo simulation and volume reconstruction.

A 1.15 mm diameter capillary tube was embedded into this phantom bordering on the surface. The total volume of the tube within a 7.5×7.5 mm^2 imaging FOV was thus 7.79 mm^3. The tube was then filled with a red dye to mimic blood at 100% HbO_2 for which the absorption coefficients at 600, 680, 780, and 875 nm were measured using a single integrating sphere. Multispectral images were acquired with the Nevoscope for the filled tube at these four wavelengths, as well as for an empty tube to serve as the background. The GA-based reconstruction procedure was randomly initialized. Since only one layer (blood) was present in the phantom, the melanin layer thickness was constrained to zero. The absorption coefficients of the blood layer in simulation, $\mu_a^{\mathrm{BL}}(\lambda)$, were modified to be the measured absorption coefficients of the red dye.

Reconstruction was performed within a $32\times32\times50$ voxel grid. The GA used a population of 100 chromosomes, with 5000 generations, 3×10^6-12×10^6 photons, a 80%-20% crossover rate, 10%-40% mutation rate, 10%-40% nudge rate, C_B=100%, $\ell_{\max}^{\mathrm{ML}} = 0$, and $\ell_{\max}^{\mathrm{BL}} = 15$. Upon completion of the reconstruction algorithm, the blood layer volume was found to be 7.02 mm^3, which matches the true tube volume with an error of 9.92%. The good reconstruction results of a single layer using images acquired with the Nevoscope give good confidence in the accuracy of the GA reconstruction on real-world images. While this phantom does not have the exact same two-layer structure of a pigmented melanin layer over-top of a blood layer as has been discussed previously, the two-layer structure was extensively simulated with the Monte Carlo simulation and GA-based reconstruction after the depth-dependent Nevoscope imaging was validated with the physical phantom. The phantom-based validated mathematical Monte Carlo simulation of a two-layer lesion for quantitative evaluation of GA-based reconstruction serves the purpose of performance evaluation and assessment of error analysis.

VII. VOLUME RECONSTRUCTION RESULTS ON REAL SKIN LESIONS

Based on the excellent simulation results for volume reconstruction, a set of 14 images of real skin lesions were obtained using the Nevoscope at a dermatology clinic. All lesions were pigmented melanocytic nevi found on light skin. Patients gave informed consent and were kept seated at rest prior to imaging. The skin lesions were inspected and classified visually by an expert dermatologist into mild, moderate, or severe categories. Multispectral transillumination images of each lesion were obtained at 600, 680, 780, and 875 nm. Images of the patient's background skin were also obtained for each wavelength to correct the lesion images for the background skin color, baseline blood perfusion, and illumination profile. These background images were taken in an area with no lesions present, typically immediately adjacent to the lesion in question.

Reconstruction was performed within a $32\times32\times50$ voxel grid. The GA used a population of 100 chromosomes, with 5000 generations, 3×10^6-12×10^6 photons, a 70%-30% crossover rate, 10%-20% mutation rate, 10%-20% nudge rate, 10%-30% intelligent nudge rate, [SO_2]=75%, $\ell_{\max}^{\mathrm{ML}} = 6$, and $\ell_{\max}^{\mathrm{BL}} = 2$. A small GA (population size of one, 10 generations, 100% intelligent nudge rate, and 3×10^6-17×10^6 photons) was used to estimate C_M (between 4% and 7%) and C_B (between

10% and 30%) based on the highest final chromosome fitness. Upon completion, a number of features were extracted from the resulting best volume estimate:

1) Lesion area, A.
2) Volume of the melanin and blood layers, V_{ML} and V_{BL}.
3) Volume of the total amount of melanin and blood, V_{M} and V_{B}, defined as $V_{\mathrm{M}} = C_{\mathrm{M}} V_{\mathrm{ML}}$ and $V_{\mathrm{B}} = C_{\mathrm{B}} V_{\mathrm{BL}}$.
4) Average melanin and blood thickness, computed as V_{ML}/A and V_{BL}/A.
5) Maximum melanin and blood depth.
6) Blood volume to total volume fraction, R, representing the volume of total blood recovered compared to the total volume of both melanin and blood, and defined as $R = V_{\mathrm{B}}/(V_{\mathrm{M}} + V_{\mathrm{B}})$.

Six lesions were classified as mild by the expert dermatologist, seven were classified as moderate, and one was classified as severe. As a result, the severe lesion was grouped together with the moderate lesions for subsequent analysis.

To assess the statistical significance of each of these volume features to differentiate between the mild class and the moderate/severe class, the non-parametric one-tailed Mann-Whitney U test was performed on each feature. The only features which were significant at the 5% significance level were the blood layer volume V_{BL} (p=0.0007), the total blood volume V_{B} (p=0.0007), the average blood thickness (p=0.001), and the highly significant blood volume fraction R (p=0.0003). All of the other features, including the total melanin volume, average melanin thickness, and maximum depths, were not significant ($p \geq$0.14). This suits the knowledge that depth by itself is not an indicator of lesion severity, since, for example, compound nevi can extend into the dermis but the vast majority are benign. Rather, it is the blood volume relative to the melanin volume which appears to be important. Despite this, it may be possible in the future to track changes to certain features over time, such as average or maximum melanin depth, to detect growth of malignant lesions early on.

Fig. 5 displays a scatter plot of average blood thickness versus the blood volume to total volume fraction R, marked with respect to class. It is clear from this figure that the mild and moderate/severe classes nicely separate into distinct clusters, with a very good potential for classification. While the severe lesion resulted in relatively large values for the average blood layer thickness and blood volume fraction, a bigger data set would be required to assess the class differences between moderate and severe with more confidence.

For a robust analysis of how well these volume features can classify the lesions into the two classes, and because the number of lesions was relatively small, a k-nearest-neighbor (kNN) classification was performed using the two most significant features: the blood volume fraction R, and the average blood thickness. For the clinical lesions, a choice of $k = 1$ was made. The test and training sets for the classifier were generated using 3-fold cross-validation.

The 3-fold cross-validated nearest neighbor classifier returned a 100% test classification accuracy for the mild and moderate/severe classes, confirming the ability of the volume features to predict lesion severity, even when the data is split into training and testing subsets. Thus, the reconstructed blood volume features demonstrate a good potential to differentiate the various levels of lesion dysplasia and severity, with an accuracy of 100% for the 14 lesions imaged.

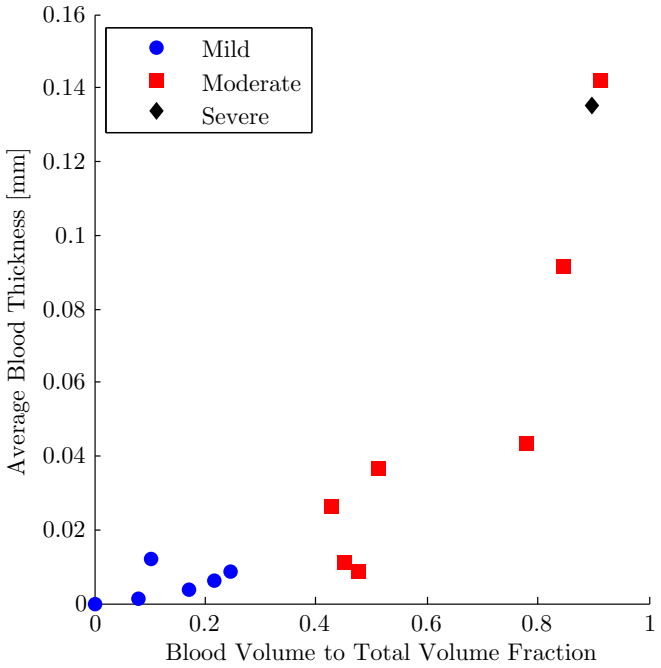

Fig. 5. Clinical lesion reconstruction features.

VIII. Conclusion

The methods presented successfully demonstrate use of features derived from volumetric reconstruction and chromophore quantification for the analysis and classification of pre-malignant lesions using multispectral imaging in a clinical setting. While further validation will need to be performed over a larger set of images, these preliminary clinical results show a promising ability to differentiate classes of lesion severity based on multispectral transillumination Nevoscope imaging with the inverse volume reconstruction algorithm. This ability could lead to fast screening, tracking, and detection of early skin cancers such as melanoma.

Acknowledgment

The authors would like to thank Dr. Babar K. Rao for his assistance in obtaining the clinical images.

References

[1] American Cancer Society, *Cancer Facts & Figures 2012*. Atlanta: American Cancer Society, 2012.
[2] R. J. Friedman, D. S. Rigel, and A. W. Kopf, "Early detection of malignant melanoma: The role of physician examination and self-examination of the skin," *CA: A Cancer Journal for Clinicians*, vol. 35, no. 3, pp. 130–151, 1985.
[3] V. Terushkin, S. W. Dusza, N. A. Mullani, M. Weinstock, R. Drugge, A. Dhawan, M. Duvic, and A. A. Marghoob, "Transillumination as a means to differentiate melanocytic lesions based upon their vascularity," *Archives In Dermatology*, vol. 145, no. 9, pp. 1060–1062, 2009.
[4] T. Gambichler, P. Regeniter, F. Bechara, A. Orlikov, R. Vasa, G. Moussa, M. Stücker, P. Altmeyer, and K. Hoffmann, "Characterization of benign and malignant melanocytic skin lesions using optical coherence tomography in vivo," *Journal of the American Academy of Dermatology*, vol. 57, no. 4, pp. 629–637, 2007.

[5] A. P. Dhawan, B. D'Alessandro, and X. Fu, "Optical imaging modalities for biomedical applications," *IEEE Reviews in Biomedical Engineering*, vol. 3, pp. 69–92, 2010.

[6] A. Goodson and D. Grossman, "Strategies for early melanoma detection: Approaches to the patient with nevi," *Journal of the American Academy of Dermatology*, vol. 60, no. 5, pp. 719–735, 2009.

[7] H. Kittler, H. Pehamberger, K. Wolff, and M. Binder, "Diagnostic accuracy of dermoscopy," *The lancet oncology*, vol. 3, no. 3, pp. 159–165, 2002.

[8] S. Tomatis, M. Carrara, A. Bono, C. Bartoli, M. Lualdi, G. Tragni, A. Colombo, and R. Marchesini, "Automated melanoma detection with a novel multispectral imaging system: results of a prospective study," *Physics in medicine and biology*, vol. 50, p. 1675, 2005.

[9] V. Wallace, D. Crawford, P. Mortimer, R. Ott, and J. Bamber, "Spectrophotometric assessment of pigmented skin lesions: methods and feature selection for evaluation of diagnostic performance," *Physics in medicine and biology*, vol. 45, p. 735, 2000.

[10] R. Marchesini, M. Brambilla, C. Clemente, M. Maniezzo, A. Sichirollo, A. Testori, D. Venturoli, and N. Cascinelli, "In vivo spectrophotometric evaluation of neoplastic and non-neoplastic skin pigmented lesions–i. reflectance measurements," *Photochemistry and photobiology*, vol. 53, no. 1, pp. 77–84, 1991.

[11] N. Tsumura, H. Haneishi, and Y. Miyake, "Independent-component analysis of skin color image," *JOSA A*, vol. 16, no. 9, pp. 2169–2176, 1999.

[12] P. Välisuo, I. Kaartinen, V. Tuchin, and J. Alander, "New closed-form approximation for skin chromophore mapping," *Journal of Biomedical Optics*, vol. 16, p. 046012, 2011.

[13] H. Zhai, H. Chan, S. Farahmand, G. Nilsson, and H. Maibach, "Tissue viability imaging: mapping skin erythema," *Skin Research and Technology*, vol. 15, no. 1, pp. 14–19, 2009.

[14] G. Monheit, A. Cognetta, L. Ferris, H. Rabinovitz, K. Gross, M. Martini, J. Grichnik, M. Mihm, V. Prieto, P. Googe, R. King, A. Toledano, N. Kabelev, M. Wojton, and D. Gutkowicz-Krusin, "The performance of melafind: a prospective multicenter study," *Archives of dermatology*, vol. 147, no. 2, p. 188, 2011.

[15] M. Moncrieff, S. Cotton, E. Claridge, and P. Hall, "Spectrophotometric intracutaneous analysis: a new technique for imaging pigmented skin lesions," *British Journal of Dermatology*, vol. 146, no. 3, pp. 448–457, 2002.

[16] E. Claridge, S. Cotton, P. Hall, and M. Moncrieff, "From colour to tissue histology: Physics-based interpretation of images of pigmented skin lesions," *Medical Image Analysis*, vol. 7, no. 4, pp. 489–502, 2003.

[17] B. D'Alessandro and A. P. Dhawan, "Depth-dependent hemoglobin analysis from multispectral transillumination images," *IEEE Transactions on Biomedical Engineering*, vol. 57, no. 10, pp. 2568–2571, 2010.

[18] L. Wang, S. L. Jacques, and L. Zheng, "MCML - monte carlo modeling of light transport in multi-layered tissues," *Computer Methods and Programs in Biomedicine*, vol. 47, no. 2, pp. 131–146, 1995.

[19] S. Wang and A. P. Dhawan, "Shape-based multi-spectral optical image reconstruction through genetic algorithm based optimization," *Computerized Medical Imaging and Graphics*, vol. 32, no. 6, pp. 429–441, 2008.

[20] B. D'Alessandro and A. P. Dhawan, "Voxel-based, parallel simulation of light in skin tissue for the reconstruction of subsurface skin lesion volumes," in *Proceedings of the 33rd Annual International Conference of the IEEE Engineering in Medicine and Biology Society (EMBC '11)*, Boston, MA, August 30 - September 3, 2011, pp. 8448–8451.

[21] N. Tsumura, M. Kawabuchi, H. Haneishi, and Y. Miyake, "Mapping pigmentation in human skin from a multi-channel visible spectrum image by inverse optical scattering technique," *Journal of Imaging Science and Technology*, vol. 45, no. 5, pp. 444–450, 2001.

[22] R. Zhang, W. Verkruysse, B. Choi, J. Viator, B. Jung, L. Svaasand, G. Aguilar, and J. Nelson, "Determination of human skin optical properties from spectrophotometric measurements based on optimization by genetic algorithms," *Journal of biomedical optics*, vol. 10, p. 024030, 2005.

[23] P. Valisuo, T. Mantere, and J. Alander, "Solving optical skin simulation model parameters using genetic algorithm," in *Biomedical Engineering and Informatics, 2009. BMEI'09. 2nd International Conference on*. IEEE, 2009, pp. 1–5.

[24] S. L. Jacques, "Skin optics," *Oregon Medical Laser Center News*, January 1998. [Online]. Available: http://omlc.ogi.edu/news/jan98/skinoptics.html

[25] S. Prahl. (1999, December 15) Optical absorption of hemoglobin. Oregon Medical Laser Center. [Online]. Available: http://omlc.ogi.edu/spectra/hemoglobin/

[26] M. J. C. Van Gemert, S. L. Jacques, H. J. C. M. Sterenborg, and W. M. Star, "Skin optics," *IEEE Transactions on Biomedical Engineering*, vol. 36, no. 12, pp. 1146–1154, 1989.

[27] B. D'Alessandro and A. P. Dhawan, "Transillumination imaging for blood oxygen saturation estimation of skin lesions," *IEEE Transactions on Biomedical Engineering*, to be published.

[28] ——, "Blood oxygen saturation estimation in transilluminated images of skin lesions," in *Biomedical and Health Informatics (BHI), 2012 IEEE-EMBS International Conference on*, Hong Kong, Shenzhen, China, January 5-7 2012, pp. 729–732.

[29] E. W. Marchand, "Derivation of the point spread function from the line spread function," *Journal of the Optical Society of America*, vol. 54, no. 7, pp. 915–919, Jul 1964.

[30] R. M. Rangayyan, *Biomedical Image Analysis*. Boca Raton, FL: CRC Press, 2005.

[31] A. P. Dhawan, *Medical Image Analysis*, 2nd ed. Hoboken, NJ: John Wiley Interscience Publications, 2011.

[32] L. Davis, *Handbook of Genetic Algorithms*. New York: Van Nostrand Reinhold, 1991.

[33] A. Garcia-Uribe, E. Smith, J. Zou, M. Duvic, V. Prieto, and L. Wang, "In-vivo characterization of optical properties of pigmented skin lesions including melanoma using oblique incidence diffuse reflectance spectrometry," *Journal of Biomedical Optics*, vol. 16, no. 2, p. 20501, 2011.

[34] M. Lualdi, A. Colombo, B. Farina, S. Tomatis, and R. Marchesini, "A phantom with tissue-like optical properties in the visible and near infrared for use in photomedicine," *Lasers in Surgery and Medicine*, vol. 28, no. 3, pp. 237–243, 2001.